Robust 60GHz Beamforming for UAVs: Experimental Analysis of Hovering, Blockage and Beam Selection

Sara Garcia Sanchez and Kaushik R. Chowdhury, *Senior Member, IEEE*

***Abstract*—Unmanned aerial vehicle (UAV) mounted millimeter wave (mmWave) base stations as well as aerial backhaul links will enable on-demand deployment of network resources. However, prior work has shown aerial links are prone to frequent disruption caused by (i) constant hovering due to GPS inaccuracies that impacts narrow beam-widths, (ii) blockages in the direct line of sight, and (iii) sub-optimal beam selection, especially if reduced angular sectors are searched in a highly dynamic environment. This paper characterizes the impact of each of these phenomena for aerial mmWave links and proposes methods to distinctly identify when they occur in isolation or in combination during deployment. Furthermore, it also proposes corrective actions at the UAV, appropriate for the specific type(s) of impacting events: physical displacement from its earlier location, angular rotation around its vertical axis, or beamwidth adjustment. Our approach relies on exploiting the information contained in the angular domain of a large dataset of experimentally collected beam-selection outcomes, under the above practical scenarios. We incorporate GPS accuracy models and antenna radiation patterns to create a robust model of potential outages. We then propose device-agnostic algorithms that jointly optimize UAVs physical movement and the beamforming procedure. Experimental results obtained by mounting a pair of 60 GHz channel sounders on M600 DJI UAVs, reveal loss reduction of up to 74.7%, translated into 260% physical layer bit-rate improvement compared to the classical 802.11ad standards-defined approach.**

***Index Terms*—obstacle detection, optimal beam, hovering, robust UAV deployments, mmWave**

I. Introduction

Millimeter wave (mmWave) frequency band (30-300 GHz) permits several GHz of channel bandwidth as compared to the congested sub-6 GHz band, resulting in Gbps data rates over the wireless channel. Despite the benefits of achieving high capacity links, such networks must be carefully deployed to cover capacity demand spikes [1]. Dense deployments of mmWave base stations can become prohibitive in terms of cost, and thus, candidate fixed infrastructure sites, such as rooftops and light-poles, cannot be selected without a lengthy planning phase. We propose the use of unmanned aerial vehicle (UAV) mounted mmWave access points that can be rapidly deployed to locations of interest. UAVs can be moved on-demand basis to adapt to the changing network traffic, as well as to connect areas impacted by disasters, where existing infrastructure is damaged, and rapid ground access may not be safe or feasible [2]. Such UAVs can form both, UAV-to-UAV backhaul links, as well as UAV-to-Ground last mile links, towards a holistic end-to-end high bandwidth connection.

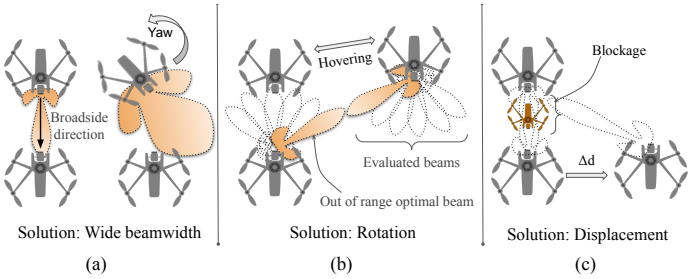

Fig. 1: Situations leading to low performance in UAV links and proposed solutions: (a) misalignment loss, (b) best out of range beam and (c) blockage.

A. Challenges in UAV mmWave Links

When a UAV is programmed to hover at a particular location, it experiences a continuous motion around the target coordinates, as UAVs often rely on inaccurate GPS signals for localization. Such hovering motion cannot be exactly predicted; our analysis shows this phenomenon to cause large impact on the communication performance leading to 91% physical layer bitrate (PHY-bitrate) drop.

Hovering impacts mmWave links in two distinct ways, mainly due to the necessity of using directed energy towards the receiver (Rx) via beamforming. First, when the beams are narrow, the resulting hovering-induced positional changes involving rotation, such as yaw, and linear motion, results in beam misalignment (see Fig.1(a)). Second, as commercial GPS resolution inaccuracy is in the order of 1-1.5 meters, the two UAVs assigned to the desired coordinates and forming an aerial link may not exactly face each other. The situation worsens when modified beamforming is used to explore a reduced angular range for decreasing latency [3] [4]. The combined effect of these two phenomena may result in the possibility that the best pair of beams, achieving the highest signal strength at the receiver among all possible angular directions (shaded in Fig.1(b)), is never evaluated. This undesirable situation may cause the selection of a sub-optimal pair of beams that continue to be maintained over time as they *appear* to be

S. Garcia Sanchez is with the Department of Electrical and Computer Engineering, Northeastern University, Boston, MA, 02120 USA (e-mail: sgarcia@coe.neu.edu).

K. R. Chowdhury is with the Department of Electrical and Computer Engineering, Northeastern University, Boston, MA, 02120 USA (e-mail: krc@ece.neu.edu).

the best among the limited, explored options. Widening the angular range, or performing a partial rotation around the UAV vertical axes are better options than settling for a sub-optimal pair of beams, which drastically decreases link performance by a factor of $\sim 100\%$ for the most severe cases.

Another challenge is the possibility of the unexpected presence of obstacles blocking the Line-of-Sight (LoS) between transmitter (Tx) and receiver [5] [6], specially in UAV-to-Ground links and when UAVs are deployed on-demand in previously unexplored areas. This can be caused by UAVs external to the network, mobile cameras, infrastructure or even human blockage (see Fig.1(c)). In our we observe that blockage causes large additional attenuation leading to an average PHY-bitrate drop of 1.45 Gbps. Moreover, recent works state that overcoming blockage in UAV links remains an open challenge [7]. It is generally difficult to assume a priori-knowledge of the deployment environment for UAVs, such as a directory of obstructions in a dynamic environment [2]. Moreover, due to the need for recharging [8], UAVs cannot remain in position beyond 0.5-1hr duration currently [9]. However, for static deployments, radios can be permanently installed in the same area, enabling environmental data collection on-site and learning [10].

Current mmWave WiFi standards 802.11ad/ay try to overcome low link performance by detecting a sudden power drop. Following this step, they initialize a beam searching procedure, in which different pairs of transmitter-receiver beams defined within a known code-book are successively swept, and their performance is evaluated [3]. After this evaluation, which we refer to as *beam-sweeping*, the protocol selects the best pair of beams for communication and this choice remains fixed until the next outage. However, if this expensive procedure that can take from hundreds of ms up to a few seconds to complete [11] (and blocks link layer traffic) is called often, there is significant impact on the overall throughput [4]. In UAV links, when power drop is caused by blockage or hovering-related mobility, repeating the beam-sweeping phase may not result in improvement [12]. For instance, in presence of blockage and the absence of alternative Non-Line-of-Sight (NLoS) paths for re-establishing the link, any new pair of chosen beams would still be affected by the obstacle. As shown in Fig.1(c), instead of a new attempt, the UAV pair has much better chance of circumventing the obstacle if they move to a slightly different location, avoiding repetitive beam-sweeping. Thus, we believe that identifying the origin of low performance can help in designing tailored solutions for each such case.

B. Contributions

The main contributions of this paper are as follows:

1) Through experiments conducted with 60GHz channel sounding equipment mounted on a pair of DJI M600 UAVs, we create a dataset of path loss collected during the beam-sweeping procedure defined by the 802.11ad protocol running on the sounder radios. We propose detection techniques for misalignment loss shown in Fig.1(a), out of range beams in Fig.1(b), and blockage due to aerial or ground-based tests in Fig.1(c). To do so, we exploit the information contained in the angular domain, applying different processing techniques to our dataset, including filtering, gradient calculation, correlation with a theoretical estimation assuming LoS using feature tracking from image processing, and supervised Machine Learning (ML) classification. We also provide a technique to determine whether link performance can be enhanced by exploiting the angular domain, otherwise avoiding unnecessary computation.
2) We introduce a stochastic analytical approach to rapidly identify the cause for link degradation when several of the effects in Fig.1 occur in combination. To this extent, and based on our experimental observations, we characterize UAV hovering displacement as a bi-modal distribution, and demonstrate its superiority compared to the Gaussian model used in the literature through measured data.
3) We design and experimentally validate a two-stage algorithm in order to (i) establish robust communication links right after UAV deployment in previously unexplored areas and (ii) re-establish performance levels in active links that experience sudden power drop.
4) We propose a method to issue a multi-modal correction that issues mobility directives as well as adapts beamforming parameters. Furthermore, our approach is formulated considering the unique impact of the above three cases of: misalignment, out-of-range beam and blockage in a stochastic sense.

The paper is organized as follows. Section II presents related work in the field. In Section III, we introduce a theoretical path loss estimation that we leverage in Section IV, where detection techniques and solutions are presented for all three effects in Fig.1, when they occur in isolation. In Section V, we extend the above methods when several effects simultaneously occur. Our proposed link recovery algorithm is given in Section VI, whereas performance evaluation is included in Section VII. We draw conclusions in Section VIII.

II. Related work

Over the last few years, a number of works aim to detect the presence of blockage in mmWave links [13] [14], while other solutions attempt to overcome its negative impact on link throughput [15] [10] [16] [3] [12]. In [15], the authors perform real-time beam readjustment after blockage detection, under the assumption of quasi-static links, by first creating a path skeleton. In [10], the authors detect and predict blockage according to historical data in a 5G cellular network. However, assuming the availability of environmental information for UAV-based systems may not always be practical. [16] proposes predictive handover to counter human blockage by using reinforcement learning and leveraging the knowledge of pedestrian locations. As it assumes the source of blockage is part of the network, this restricts the applicability of the solution to specific scenarios. [3] performs out-of-band inference to reduce in-band overhead for establishing the best directional mmWave beam in presence of blockage. While the results are promising in their implementation, the setup requires additional wireless hardware that impacts UAV load capacity and battery constraints. [14] is the closest work to our approach

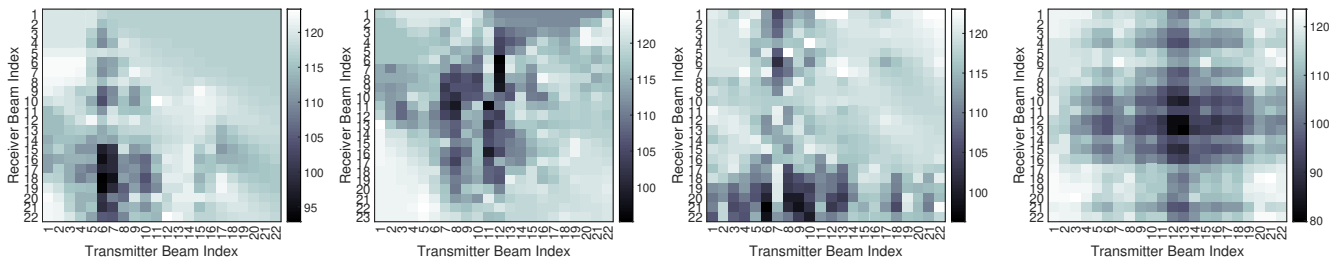

(a) LoS, hovering (b) Blockage (c) Out of range (d) LoS, static

Fig. 2: Experimental path loss angular distribution l_E for (a),(b),(c) three UAV-to-UAV scenarios and (d) a static case.

on obstacle detection that assumes neither environmental information nor additional hardware. The radio monitors a single beam link over time, and associates blockage with Signal to Noise Ratio (SNR) drop in static environments. However, hovering-related motion in UAV links also causes power drops, which are comparable to the attenuation produced by strong blockages [17]. Thus, the approach in [14] may lead to false positives. In [12], the authors determine whether link quality drop is due to mobility or blockage and present simulation results for different ML algorithms. They conclude the need of offline training data in order to achieve high accuracy, not practical for UAV scenarios. In addition, assumptions such as, error-free GPS localization data or imported diffraction models from sub-6GHz equations applied to mmWave, need to be experimentally validated in real systems. Moreover, none of the aforementioned works focus on detecting, identifying, and addressing the cause for low link performance specific to point-to-point UAV links.

Specific to UAV communication, several works have studied robust and dynamic deployments [18], positioning for flexible coverage [19] [20] and presence of blockage and impact of directionality through simulations [5] [6]. The work in [5] relies on UAVs in order to create alternative mmWave links to overcome blockage, whereas [6] uses multi-UAV coordination to maximize the achievable sum-rates in presence of obstacles. Instead, our focus is to ensure robust deployment and operation for a single UAV point-to-point link, without any supporting network infrastructure. In [21], the authors present simulation results for beam tracking in vehicular communications to overcome obstacles by leveraging information contained in the angular domain. Other recent works on UAV-mmWave communications recognize the importance of including blockage in their formulations [22], and propose to consider this in their future work.

III. Theoretical Estimation of Path Loss Angular Distribution

In order to identify the cause for observed low link performance, our proposed solution exploits the information contained in the angular domain for the path loss data collected during the standard beam-sweeping procedure, denoted as l_E, and compares it with a theoretical estimation l_T. For an intuitive feel of this approach, consider the plots in Fig.2, showing l_E for LoS conditions during hovering (a), blockage (b), best out of range beam (c), and LoS conditions for a static setup (d). The x-axis represents beam index for transmitter $m_{tx} = \{1...M_{tx}\}$ and y-axis for the receiver $m_{rx} = \{1...M_{rx}\}$, where M_{tx}, M_{rx} are their respective total number of beams. Each beam index corresponds to a different angular direction in the azimuth dimension θ, which we call as beam *pointing angle*. Thus, Fig.2 shows the measured path loss l_E for a total of $P_M{=}M_{tx}M_{rx}$ pair of beams evaluated during beam-sweeping. This data also includes the pair of beams p_{ms} that are finally chosen after beam-selection concludes. Our hypothesis is that the information contained in l_E is sufficient to distinguish the cause for low performance in UAV links, for all the scenarios in Fig.1.

In order to test the above hypothesis, we next present the theoretical estimation of the angular distribution of path loss l_T that corresponds to the outcomes shown in Fig.2. This estimation provides angular data for $P_N{=}N_{tx}N_{rx}$ pair of beams, under the assumption of LoS conditions. We then use this estimation in our proposed algorithm to (i) identify whether low performance can be mitigated by exploiting the angular domain, and (ii) apply our blockage detection method. We provide a table of notations (Table X), at the end of the manuscript.

A. Estimation of Angular Path Loss Distribution

We perform our estimation in two steps:

1) Approximated Free Space Path Loss (FSPL) Calculation: Using the distance between transmitter and receiver from GPS measured coordinates $\widetilde{d}$, we first calculate $\widetilde{FSPL}$, as the estimated FSPL, which remains constant for all P_N pair of beams. The FSPL error bounds for a given $\widetilde{d}$ due to GPS error is denoted as ϵ_T. Thus, we use the distance range bounded by $\widetilde{d} \pm \epsilon_T$ in our $\widetilde{FSPL}$ calculation.

2) Angular Refinement: We then refine the estimated $\widetilde{FSPL}$ value for each pair of beam considered for the theoretical estimation. To do so, we include additional misalignment loss as beams point to different angular directions during the beam-sweeping procedure. We illustrate this in Fig.3 (a), where transmitter and receiver radios sweep their beams over three different angular directions, evaluating a total of nine pair of beams. For each evaluated pair, l_{tx} and l_{rx} represent additional loss compared to perfect alignment at transmitter and reciever sides. This alignment condition occurs when transmitter and receiver point towards their *broadside direction* θ_{bs} (maximum of radiation pattern normal to the plane containing the array), being $\theta_{bs} = 0°$ under the assumption that transmitter and receiver are perfectly aligned and facing each other. In Fig.3 (a), maximum alignment corresponds to

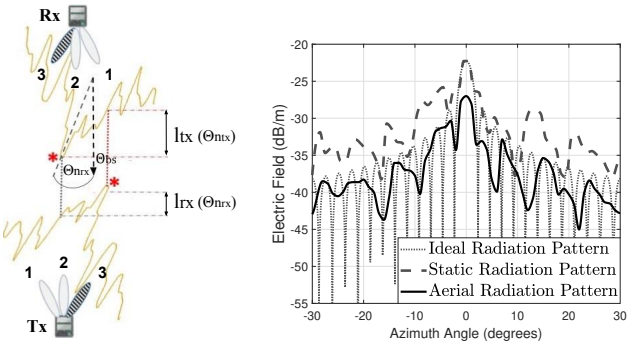

(a) (b)

Fig. 3: (a) Misalignment loss for transmitter l_{tx} and receiver l_{rx} for beams (3-3), compared to perfect beams alignment for beams (2-2) which point towards the antenna broadside direction, normal to the plane containing the array, θ_{bs}= 0°. (b) Ideal, Static and Aerial radiation patterns, θ_{3dB}=2.8°.

the case when transmitter and receiver are both evaluating the performance for pair of beams 2. Thus, we use the difference between the estimated path loss in this case and the estimated path loss for all other eight pair of beams to build l_T. Given the high dependency of l_{tx} and l_{rx} on antenna radiation pattern $f_{tx}(\theta), f_{rx}(\theta)$, we characterize and incorporate them in our theoretical estimation.

B. Proposed Antenna Radiation Pattern Characterization

Phased arrays are commonly used to provide analog beamforming gain at mmWave frequencies [2]. We use antenna array synthesis to estimate the spatial distribution of the electric field, with knowledge of the phase values for each array element and the antenna configuration. For azimuth steering, horizontal polarization, uniform amplitude and spacing, and assuming all elements as equal and no coupling between elements, we estimate the total electric field E_T as [23]

$$E_T = E_0(AF) = E_0(\sum_{s=1}^{S} e^{j(s-1)(\frac{2\pi f}{c} d_s cos\theta + \beta)}), \quad (1)$$

where the E_T radiated by S elements is a function of the electric field radiated by a single element E_0 and the Array Factor (AF). The latter depends on the difference in phase excitation between radiating elements β, and their separation distance d_s, where c is the speed of light in vacuum. Alternatively, the antenna radiation pattern function can be numerically calculated by using electromagnetic analysis software packages [24]. These methods approximate the electromagnetic field by solving Maxwell equations on multiple small regions of an antenna three-dimensional (3D) model, for which, the electromagnetic field in each region is assumed to be constant.

For maximum accuracy, we measure the antenna radiation pattern in a radio frequency (RF) anechoic chamber by emulating flying conditions, for a discrete set of angles $\theta \in \mathbb{Z}$ in the range of $[-30°, 30°]$ and angular resolution of 1°.

We mount the transmitting channel sounder on the UAV and turn the rotors on. The receiver channel sounder is mounted on a tripod. We compare the measured radiation pattern with a setup in which both channel sounders are mounted on tripods. We observe additional losses of 9.5 dB for the former case due to signal reflection from the UAV airframe, which we denote as L_{Afr}. We show both radiation patterns in Fig.3 (b), along with an ideal beampattern simulated according to (1).

Given hardware-related effects, the antenna radiation patterns $f_{tx}(\theta), f_{rx}(\theta)$ do not remain constant as the main lobe points to different angular directions during beam-sweeping [24]. Thus, a total of $N_{tx} + N_{rx}$ radiation patterns must be characterized for an accurate loss estimation. To minimize overhead, we only characterize the central beam at the transmitter side and assume all other beams are equal. We also study the impact of this approximation on the accuracy achieved by our solution.

C. Path Loss Estimation

Next, we provide a formal definition for the theoretical path loss estimation l_T, according to the following system parameters: the operation frequency f_c, GPS distance between transmitter and receiver $\widetilde{d}$, and GPS error ϵ_T, which define the estimated $\widetilde{FSPL}$, the available antenna radiation patterns $f_{tx}(\theta), f_{rx}(\theta)$, the total number of pair of beams considered on the theoretical estimation P_N, the angular step between consecutive pair of beams δ, and the airframe-related loss L_{Afr}.

We refer to each of the P_N pair of beams by their beam indices (n_{tx},n_{rx}) or by their pointing angles ($\theta_{n_{tx}}$,$\theta_{n_{rx}}$), for transmitter and receiver respectively. We denote the best pair of beams over l_T as p_{ns}, with pointing angles ($\theta_{ns_{tx}}$,$\theta_{ns_{rx}}$).

The pointing angles are a function of the beam-sweeping angular step δ and the beam-sweeping angular range θ_r, this is $\theta_{n_{tx}} = \delta(n_{tx}) \in \theta_r$ with $n_{tx} \in \mathbb{Z}^+$. In order to consider the angular step as metric for spatial resolution, we ensure $\delta(n_{tx})$,$\delta(n_{rx}) \in \mathbb{R}^+ \cup \{0\}$, and define it as

$$\delta(n_{tx}) = \begin{cases} \theta_{n_{tx}} - \theta_{n_{tx}-1}, & n_{tx} - ns_{tx} > 0 \\ \theta_{n_{tx}} - \theta_{n_{tx}+1}, & n_{tx} - ns_{tx} < 0 \\ 0, & n_{tx} - ns_{tx} = 0. \end{cases} \quad (2)$$

Note that the last case ensures transmission in the broadside direction. Taking a step function with constant angular step $\delta(n_{tx}) = \delta$, we define the pointing angles as

$$\theta_{n_{tx}} = \delta(n_{tx} - ns_{tx}) \in [\delta(\frac{1-P_N}{2}), \delta(\frac{P_N-1}{2})]. \quad (3)$$

We estimate misalignment loss at the transmitter side l_{tx} for pointing angle $\theta_{n_{tx}}$ as the difference between the transmitter antenna radiation pattern f_{tx}, evaluated at $\theta_{n_{tx}}$, and its maximum value corresponding to $f_{tx}(\theta_{bs})$,

$$l_{tx}(\theta_{n_{tx}})[dB] = f_{tx}(\theta_{bs}) - f_{tx}(\theta_{n_{tx}}). \quad (4)$$

Misalignment loss at the receiver side $l_{rx}(\theta_{n_{rx}})$ is obtained from an equivalent expression of (4).

We estimate the total path loss for a pair of beams with pointing angles ($\theta_{n_{tx}}$,$\theta_{n_{rx}}$) in a UAV-to-UAV link as

$$l_T(\theta_{n_{tx}}, \theta_{n_{rx}}) = \widetilde{FSPL} + 2L_{Afr} + l_{tx}(\theta_{n_{tx}}) + l_{rx}(\theta_{n_{rx}}), \quad (5)$$

where the addition of the last two terms correspond to total misalignment loss. The airframe-induced loss is $2L_{Afr}$, as

both transmitter and receiver are mounted on UAVs. We scale it down by a factor of 2 for UAV-to-Ground links. Notice that when transmitter and receiver beams point towards the broadside direction, $\theta_{n_{tx}}, \theta_{n_{rx}} = \theta_{bs}$, misalignment losses $l_{tx}(\theta_{n_{tx}}), l_{rx}(\theta_{n_{rx}})$ are null, and the loss for this particular pair of beams is simply given by $\widetilde{FSPL}$ and L_{Afr}, according to (5). The latter can be derived from the spatial data obtained during initialization, as discussed in Section IV-A. This is, the difference between $FSPL$ for a reference distance and the measured value, when beams are perfectly aligned and under LoS conditions.

In Fig.4(a), we show the result of our theoretical estimation using the aerial radiation pattern presented in Fig.3(b) for a total of 1024 different pair of beams. We consider an angular range $\theta_r = [22.4°, 23.8°]$ and a constant angular step $\delta = \frac{\theta_{3dB}}{2}$ of 1.4°, where θ_{3dB} is the antenna half-power beamwidth. We approximate the centroid of the measured cluster as the point of minimum path loss, corresponding to the pair of beams achieving best alignment.

D. Experimental Validation

In order to validate our theoretical formulation, we contrast l_T with experimental data collected for two different outdoor open environments under LoS conditions, a grassland open-area shown in Fig.2(d), and a parking lot. In both cases, we perform beam-sweeping with the channel sounders separated a distance of 6 meters, facing each other.

In Fig.4(b), we compare l_T with the measured path loss in both scenarios. The theoretical path loss estimation error is calculated for a distance deviation of $\epsilon_T = \pm 1.5$ meters, as this is the maximum longitudinal displacement a M600 UAV model can experience, as we later discuss in Section V-B1. The experimental path loss error ϵ_E is hardware related, with a value of up to 4 dB. The x-axis has ordered pair of beams for increasing path loss according to the theoretical model. Thus, the left side of the plot contains the pair of beams closer to the centroid of the cluster. We apply a moving filter to the experimental data to smooth measurement errors and view general trends. We observe that l_T is accurate for the pair of beams close to the centroid. The divergence at the extremities is due to increased difference between radiation patterns as we move far from the central beam that we characterized.

In the next section, we present our proposed solution that leverages the theoretical estimation of l_T described here. Furthermore, we propose a simple solution to detect and re-establish best-case link performance.

IV. Ensuring Resilient Link Performance

In Fig.1, we described the main reasons for low performance in mmWave UAV links as (a) misalignment loss, (b) best out of range beam selection, (c) presence of blockage between transmitter and receiver, or a combination of them. In this section, we design detection and solution techniques for each of these three effects if they occur in isolation. To do so, we leverage the theoretical estimation given in Section III, and exploit the information contained in the angular dimension of the in-flight experimental path loss data collected. Then,

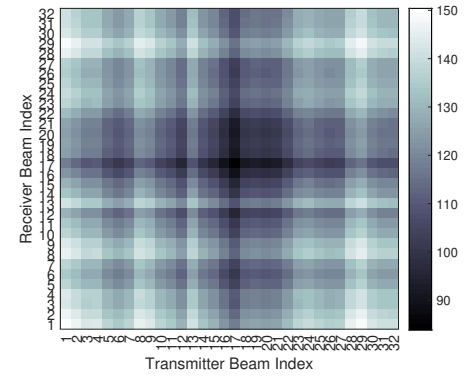

(a)

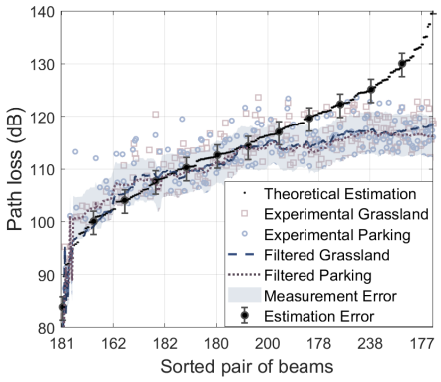

(b)

Fig. 4: (a) Theoretical path loss estimation l_T for 1024 pair of beams. (b) Experimental validation of l_T.

in Sections V and VI, we extend our approach to scenarios where multiple effects happen simultaneously, through a low complexity solution.

A. Input Parameters

Our approach assumes no knowledge of the obstacle location and no prior environmental information. Our inputs are:

1) Theoretical estimation of the path loss angular distribution: as we described in Section III. We use l_T for obstacle detection (IV-D), and solution triggering (V-A).

2) GPS approximated location data: This gives a rough estimation for $\tilde{d}$, that we use to perform beamwidth adjustment to existing hovering conditions (IV-B).

3) Experimental path loss angular distribution in an open-environment, under LoS conditions: based on the data we show in Fig.2(d). This is required as a one-time initialization step, subject to the change of major operational conditions, such as hardware. We discuss further this issue in Sections IV-C and IV-D.

We next present the individual solutions for the different causes of performance degradation.

B. Misalignment Loss

The first effect we aim to overcome is misalignment loss caused by the use of directional beams under hovering conditions. Even when the best beam-pairs are selected in the absence of blockage, misalignment loss still causes drastic power

drop. Our solution involves adjusting the antenna beamwidth based on current hovering conditions as

$$\theta_{3dB} = 2atan(\frac{max\{\Delta d\}}{\widetilde{d}}), \quad (6)$$

where Δd is the hovering displacement range (range of motion as the UAV hovers around the targeted coordinates), that we later characterize in Section V-B1. We provide guidance on which value should be assumed in Sections V-B4 and VI-A.

C. Best Out of Range Beam

The second effect we consider is illustrated in Fig.1(b), which we refer to as *out of range*. To detect this situation, we rely on information contained within the path loss angular distribution of experimental data l_E. In particular, under out of range conditions, the centroid of l_E is not part of the collected data (see Fig.2(c)). For detection, we propose to analyse the decreasing behavior of l_E with respect to the transmitter and receiver pointing angles $(\theta_{m_{tx}}, \theta_{m_{rx}})$. To this extent, we calculate the averaged value of the projection of the negative gradient vector of l_E over each pointing direction $\theta_{m_{tx}}, \theta_{m_{rx}}$, where l_E is considered as a 2D discrete function. For the transmitter case,

$$\bar{\nabla l_{E(\theta_{m_{tx}})}} = \frac{\sum_{\theta_{m_{tx}}} < \hat{\theta_{m_{tx}}}, -\nabla l_E(\theta_{m_{tx}}, \theta_{m_{rx}}) >}{P_M}, \quad (7)$$

which is equivalent for the receiver $\bar{\nabla l_{E(\theta_{m_{rx}})}}$, where $\hat{\theta_{m_{tx}}}, \hat{\theta_{m_{rx}}}$ are the transmitter and receiver pointing unit vectors, ∇ is the gradient operator, $<,>$ the inner product operator, and $-\nabla l_E$ is the direction that results in the greatest decrease in path loss. Since we are interested in the angular distribution tendency of l_E caused by potential out of range situations, we filter l_E prior to calculating the gradient. This minimizes the effect of the radiation pattern (and potential presence of obstacles) on the calculated gradient.

According to (7), a positive value of $\bar{\nabla l_{E(\theta_{m_{tx}})}}$ implies that the averaged value of the negative gradient over all P_M pair of beams, points to the positive angular region of the transmitter $+\hat{\theta_{m_{tx}}}$. Thus, there is a tendency for l_E to decrease towards this angular direction, where we expect the centroid to be located. Analogously, for negative values of $\bar{\nabla l_{E(\theta_{m_{tx}})}}$, the centroid is expected to be located towards the negative angular region of the transmitter $-\hat{\theta_{m_{tx}}}$. This reasoning is equivalent for $\bar{\nabla l_{E(\theta_{m_{rx}})}}$ at the receiver side. In this case, our proposed solution involves rotating the transmitter and/or receiver UAVs toward the direction where the centroid is expected to be, to maintain the same pair of beams and thus, avoid breaking the communication link. If $\bar{\nabla l_{E(\theta_{m_{tx}})}}, \bar{\nabla l_{E(\theta_{m_{rx}})}}$ are null, we conclude that the averaged value of $-\nabla l_E(\theta_{m_{tx}}, \theta_{m_{rx}})$ in each dimension is compensated over all pair of beams, in which case, the centroid is located at the middle of l_E, and thus, rotation is not required.

In order to avoid rotation when $\bar{\nabla l_{E(\theta_{m_{tx}})}}, \bar{\nabla l_{E(\theta_{m_{rx}})}}$ are not null but ~ 0, we estimate both values for the experimental path loss angular distribution required as input mentioned in Section IV-A3, where transmitter and receiver are facing each other. We only start the UAV rotation for values much higher (x10 times) than the calculated values that we set as thresholds $\xi_{th(tx)}, \xi_{th(rx)}$. In Table I, we summarise required actions according to different conditions, where rotation to $+\hat{\theta_m}, -\hat{\theta_m}$ correspond to clockwise and counter-clockwise UAV motion respectively.

TABLE I: Out of Range Solution

Condition	Action: Rotation
$\mid \nabla l_{E(\theta_{m_{tx}})} \mid > \xi_{th(tx)}, \quad -\nabla l_{E(\theta_{m_{tx}})} > 0$	Transmitter to $+\hat{\theta_{m_{tx}}}$
$\mid \nabla l_{E(\theta_{m_{tx}})} \mid > \xi_{th(tx)}, \quad -\nabla l_{E(\theta_{m_{tx}})} < 0$	Transmitter to $-\hat{\theta_{m_{tx}}}$
$\mid \nabla l_{E(\theta_{m_{rx}})} \mid > \xi_{th(rx)}, \quad -\nabla l_{E(\theta_{m_{rx}})} > 0$	Receiver to $+\hat{\theta_{m_{rx}}}$
$\mid \nabla l_{E(\theta_{m_{rx}})} \mid > \xi_{th(rx)}, \quad -\nabla l_{E(\theta_{m_{rx}})} < 0$	Receiver to $-\hat{\theta_{m_{rx}}}$

D. Blockage

Although the presence of an obstacle in the LoS path cannot be detected by evaluating a single pair of beams, as discussed in Section II, we can infer such a condition by exploiting information in the angular domain. In our approach, we compare the in-flight measured path loss angular distribution l_E (e.g in Fig.2), with the theoretical estimation l_T (Fig.4(a)), calculated according to Section III. Since we estimate l_T assuming LoS conditions, the degree of similarity between estimation and measurement is the metric we use to identify whether the link is established under LoS conditions, or suffers from blockage.

1) Normalized Cross-Correlation as Similarity Metric: Given that l_T and l_E do not necessarily have the same dimension, we quantify their degree of similarity as the maximum value of the normalized cross-correlation between them. We adapt this approach from feature tracking in image processing [25].

We consider an image (l_E) of dimension $M_{tx} \times M_{rx}$, and a feature (a subset of the theoretical data l_T) of dimension $N_{tx} \times N_{rx}$, being $M_{tx} \geqslant N_{tx}, M_{rx} \geqslant N_{rx}$. The roles of l_E and l_T as image and feature are interchangeable. However, we prefer to limit the size of l_T, considering it as feature, as it suffers from estimation errors as we move away from its centroid due to the lack of a full characterization for all radiation patterns, as illustrated in Fig.4(b). The approach is based on the Euclidean distance, defined as

$$d^2_{l_E,l_T} = \sum_{\theta_m} [l_E(\theta_m) - l_T(\theta_m - \theta_w)]^2, \quad (8)$$

where $\theta_m = (\theta_{m_{tx}}, \theta_{m_{rx}})$ are the pointing angles for the image, and $\theta_w = (\theta_{w_{tx}}, \theta_{w_{rx}})$ is the position of a window w containing the feature. The sum in (8) is performed over the image pointing angles within the window. The normalized cross-correlation for a given θ_m, θ_w is then defined as

$$x_{cross} = \frac{\sum_{\theta_m} [l_E(\theta_m) - \bar{l}_{E_{\theta_w}}][l_T(\theta_m - \theta_w) - \bar{l}_T]}{\{\sum_{\theta_m} [l_E(\theta_m) - \bar{l}_{E_{\theta_w}}]^2 \sum_{\theta_m} [l_E(\theta_m) - \bar{l}_{E_{\theta_w}}]^2\}^{0.5}}, \quad (9)$$

where $x_{cross} \in \mathbb{R}$, and $\bar{l}_{E_{\theta_w}}$ and $\bar{l}_T$ are the averaged experimental and theoretical path loss respectively, calculated within the window where the feature l_T is located. The result $\forall \theta_m, \theta_w$ is the matrix $X_{cross} \in \mathbb{R}^{(M_{tx}+N_{tx}-1, M_{rx}+N_{rx}-1)}$.

In feature tracking, maximum cross-correlation occurs when the feature is aligned with itself on the image. In our case, maximum cross-correlation occurs under LoS conditions, where the centroids of l_T and l_E are aligned. However,

TABLE II: Radiation Pattern Effect on $\max\{X_{cross}(l_T, l_E)\}$

Scenario	Aerial Radiation Pattern	Ideal Radiation Pattern
Grassland	0.808	0.698
Parking Lot	*0.812*	0.631

when blockage occurs, the centroid of the latter is obscured, causing correlation to drop. This does not even guarantee that maximum cross-correlation corresponds to proper alignment between feature and image. Thus, from the maximum value of the normalized cross-correlation matrix X_{cross} over all pointing angles θ_m, θ_w, calculated from (9), we determine whether links are established under LoS or blockage conditions.

Our motivation to use (9) as similarity metric is due to several reasons: First, this approach is robust against measurement anomalies, as it does not consider a single data point for determining maximum similarity, but rather, leverages angular information from multiple pair of beams. Second, normalization allows for comparison, which is required for obstacle detection. Third, the subtraction of the path loss average values $\bar{l}_{E_{\theta_w}}, \bar{l}_T$, makes x_{cross} invariant to changes in the image power all pixels are equally affected [25], or in our case, all P_N pair of beams. This is crucial, as errors in l_T are expected, such as FSPL estimation errors caused by relying on inaccurate localization system measurements, or by not considering the effect of unfavorable weather conditions, as we later discuss in Section V-A, among others.

2) Parameters Affecting Cross-Correlation: In order to distinguish between LoS and blockage conditions from the x_{cross} value, we first analyse its dependency with the antenna radiation pattern, data dimension and multipath conditions:

- Radiation Pattern. Although the normalized cross-correlation x_{cross} defined as in (9) is not affected by errors equally affecting all P_N pair of beams, its value is subject to local errors, i.e., those affecting a limited region of l_T. Moreover, since l_T relies on the knowledge of the antenna radiation pattern, if we fail to accurately characterize its angular power distribution, the correlation value between estimation and measurement drops. To illustrate this, we present in Table II the maximum value of the cross-correlation matrix $\max\{X_{cross}(l_T, l_E)\}$ for the grassland and parking scenarios, already introduced in Section III-D, for the aerial and ideal radiation patterns shown in Fig.3(b). As the ideal radiation pattern locally differs from the real case, correlation drops. The correlation value for the aerial radiation pattern can be brought closer to 1 with a full characterization of all pair of beams for transmitter and receiver, as we stated in Section III-B.
- Data Dimension. We can reduce the data dimensions in the image l_E, either by reducing the angular beam-sweeping range θ_r or by increasing the angular step between two consecutive beams δ. However, limiting the number of beams evaluated during beam-sweeping or the angular resolution, decreases the amount of information available in the angular domain. This affects centroid alignment between image l_E and feature l_T under LoS conditions, and thus, decreases maximum correlation achieved in the absence of blockage. A better approach to reduce data dimension is by considering a subset of the theoretical path loss estimation l_T, specially if our radiation pattern characterization lacks accuracy. In Fig.5, we show the $\max\{X_{cross}(l_T, l_E)\}$ value for different l_T data dimension, for the grassland scenario. The squared area corresponds to successful centroids alignment within a an angular resolution of $\delta = 1.4°$. Notice that maximum correlation is achieved for the lowest possible dimension, however, centroid alignment is not successful. In Table III, we show the dimensions with proper alignment and the corresponding correlation between aerial and ideal radiation patterns. Since the aerial radiation pattern is a better characterization, less data is sufficient to ensure centroid alignment and high correlation under LoS. For similar reasons, and since the radiation pattern we characterized is on the transmitter side (see Section III-B), receiver data dimension in the aerial case is higher compared to transmitter.

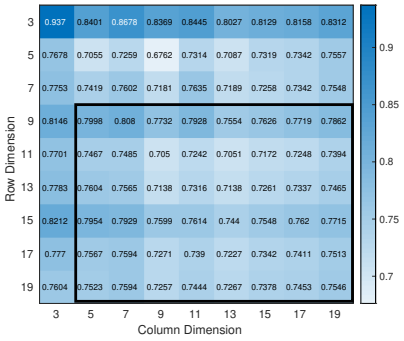

Fig. 5: $\max\{X_{cross}(l_T, l_E)\}$ as function of l_T dimension.

TABLE III: Data Dimension Effect on $\max\{X_{cross}(l_T, l_E)\}$

Radiation Pattern	Data Dimension ($N_{rx} \times N_{tx}$)	$max\{X_{cross}(l_T, l_E)\}$
Aerial	9x7	0.808
Ideal	*9x9*	0.804

- Multipath. In presence of rich multipath, commonly expected in UAV-to-Ground links, the measured data l_E does not only depends on the antenna radiation pattern and data dimension, but also on the presence of scatterers, their locations, shapes and materials [2]. We illustrate this effect in Fig.6, comparing l_E for measured path loss between (a) an open environment and (b) a scenario where there exits a nearby wall causing reflection. Since multipath caused by the wall locally alters the path loss angular distribution, it is an additional factor -other than blockage-, causing correlation drop. Thus, as the theoretical path loss estimation given in Section III assumes LoS, the correlation drop caused by multipath could be interpreted as the presence of an obstacle, leading to false positives for blockage detection. To overcome this, we propose the use of a simple supervised ML method, described next. With this approach, data collected during multiple deployments is leveraged to enhance the obstacle detection accuracy in the longer term.

3) Naïve Bayes Classifier for Obstacle Detection: In this section, we propose the use of a binary classifier in order to distinguish between LoS ($class_1$ = 'LoS') and blockage ($class_2$ = 'block'). We collect labelled $\max\{X_{cross}(l_T, l_E)\}$ values during multiple deployments to create a dataset of

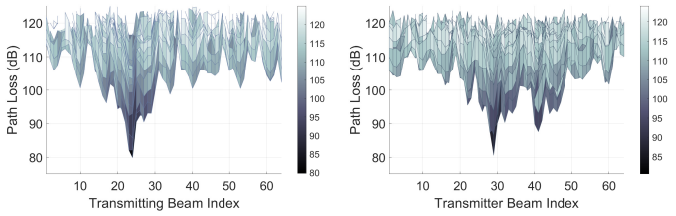

(a) (b)

Fig. 6: Measured path loss for (a) open and (b) rich multipath environments, for all transmitter beams, broadside at receiver.

observations $\mathcal{D}$. We then use a simple supervised ML approach to classify new values into one of the two classes. We chose Naïve Bayes classifier, as it requires small amount of data to achieve high accuracy and returns classification probabilities as confidence metric. Since our method has a single feature, $\max\{X_{cross}(l_T, l_E)\}$, the independence assumption holds. From Bayes theorem, the posteriori probability of blockage $P(block|\mathcal{D})$ based on the dataset of observations $\mathcal{D}$ is given by

$$P(block|\mathcal{D}) = \frac{P(\mathcal{D}|block)P(block)}{P(\mathcal{D})}, \tag{10}$$

with $P(\mathcal{D}|block)$ the likelihood function, $P(block)$ the prior probability of blockage, and $P(\mathcal{D})$ the evidence. (10) is equivalent for the 'LoS' class. We then determine

$$\begin{cases} LoS: \quad if \quad P(LoS|\mathcal{D}) \geqslant P(block|\mathcal{D}) \\ Blockage: \quad if \quad P(LoS|\mathcal{D}) < P(block|\mathcal{D}). \end{cases} \tag{11}$$

V. Identifying Causes of Link Degradation

In Section IV, we proposed detection techniques and solutions for all three effects presented in Fig.1, when they happen in isolation. However, a combination of these effects may simultaneously happen. Moreover, low link performance may also be caused by other factors such as air moisture, rain or ground absorption in UAV-to-Ground links, which we do not model in our work so far. Thus, our approach first involves (A) solution triggering, which determines whether or not our solutions are applicable for enhancing link performance. If so, a second step (B) performs an analytical estimation that determines which of the different effects in Fig.1 may be likely causing low performance, and thus, which techniques from Section IV we should prioritize. The specific steps of the algorithm are given in Section VI.

A. Solution Triggering

External environmental conditions affect equally all pair of beams or angular directions, and thus, our solutions (motion, rotation, or beamwidth increase) are not expected to result in meaningful gains. From the similarity metric defined in (9) in Section IV-D1, the x_{cross} value is invariant to changes on the image power, when changes equally affects all pair of beams. Thus, when low performance is detected, and yet, the $\max\{X_{cross}(l_T, l_E)\}$ value is high, link degradation is caused by an effect producing the same power drop on all pair of beams. In this case, we choose not to trigger further

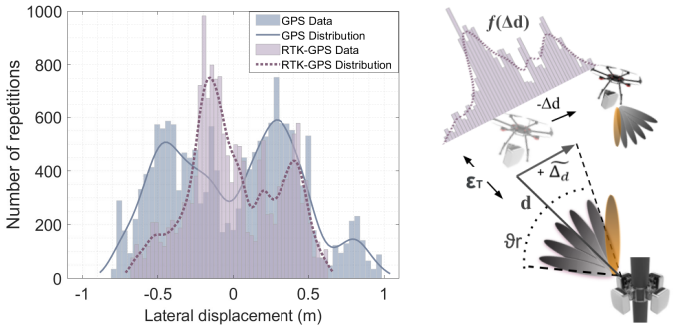

(a) (b)

Fig. 7: (a) UAV displacement in lateral dimension under moderate hovering conditions, flight-time of 9 minutes. (b) Parameters for calculation of P_{oR}.

TABLE IV: Hovering Range Characterization

Hovering conditions	$\Delta d(m)$	Source
Moderate	$[-0.6, 0.6]$	Experimental
Strong	$[-1.5, 1.5]$	Specifications

calculations. On the contrary, when the $\max\{X_{cross}(l_T, l_E)\}$ value is low, link degradation is caused by an effect that locally alters the path loss angular distribution.

In contrast with the cases where different effects occur in isolation (see Section IV), when several effects simultaneously occur, low values of $\max\{X_{cross}(l_T, l_E)\}$ are not necessarily associated with blockage. Out of range may also be the cause for a *hidden* centroid, when the centroid is not part of the experimental path loss distribution that leads to a drop in correlation. Since the cause for low $\max\{X_{cross}(l_T, l_E)\}$ values may be blockage, out of range, or a combination of both, we need to rapidly identify the cause for link degradation.

B. Stochastic Analytical Approach

Next, we provide a hovering characterization used to derive closed-form expressions for the probabilities of blockage, LoS, best out of range beam, and insufficient beamwidth for given hovering conditions, based on in-flight parameters available during operation.

1) Hovering Characterization: To derive a stochastic expression for UAV hovering, we first characterize the hovering displacement range Δd for what we denote as *moderate* hovering conditions, which are conducive for safe and reliable operation. To this extent, we collect UAV localization data for scenarios with no buildings within a radius of 15 meters, strong satellite signal reception (SNR >35 dB) from at least 4 satellites, and maximum wind speed of 17 miles/hour. For enhanced accuracy in the hovering characterization, we collect data using an EMLID Real-Time Kinematic GPS (RTK-GPS) unit, which uses averaged measurements from a ground station in order to correct GPS error achieving cm-level accuracy. Additionally, we provide the maximum Δd for what we denote as *strong* hovering conditions, determined by the maximum hovering the DJI M600 model experiences, according to its specifications [26]. Table IV shows the Δd value for both cases, applicable to linear motion along lateral and longitudinal dimensions.

Once Δd is characterized, we formulate a stochastic model for it. Recent works assume hovering follows a Gaussian distribution [27], given by

$$\Delta d \sim \mathcal{N}(\mu, \sigma^2), \tag{12}$$

with mean μ centered at the true UAV coordinates and typical deviation $\sigma = (\frac{max\{\Delta_d\}}{3})$ related to the maximum hovering displacement range.

In contrast, our experimental observations show that hovering is better modeled as a bimodal distribution, similar to GPS [28] for the limited UAV flight-time (typically $<$ 10-12 minutes with load in our case). We prove this in Fig.7(a), where we show collected hovering data using a RTK-GPS unit. The signal distribution is contrasted with lower accuracy UAV-mounted GPS sensor data collected during the same experiment. Thus, we characterize hovering as a dual-mode Gaussian Mixture Model (GMM), with probability density function given by [29]

$$\Delta d \sim v_1\mathcal{N}(\mu_1, \sigma_1^2) + v_2\mathcal{N}(\mu_2, \sigma_2^2), \tag{13}$$

with $v_1 + v_2 = 1$, and where μ_1, μ_2 are each mode means, and σ_1, σ_2 selected such that $[\mu_1 - 3\sigma_1, \mu_2 + 3\sigma_2] = [-max\{\Delta_d\}, max\{\Delta_d\}], \mu_1 \leqslant \mu_2$, to ensure maximum hovering range follows values in Table IV. Given the unpredictable nature of GPS signals, the mean values μ_1, μ_2 are randomly located within Δd. According to their location, the lower bound for hovering displacement corresponds to

$$\Delta d \sim 0.5\mathcal{N}(\mu, \frac{max\{\Delta_d\}}{3}^2) + 0.5\mathcal{N}(\mu, \frac{max\{\Delta_d\}}{3}^2), \tag{14}$$

with μ as the true coordinates. We note that this case is equivalent to a Gaussian distribution with $\sigma = \frac{max\{\Delta_d\}}{3}$. Moreover, the upper bound for hovering displacement corresponds to a bimodal distribution where the separation between μ_1, μ_2 is maximum. Considering a minimum hovering range $\Delta_{d_{min}}$,

$$\Delta d \sim v_1\mathcal{N}(\mu_1, \Delta_{d_{min}}^2) + v_2\mathcal{N}(\mu_2, \Delta_{d_{min}}^2), \tag{15}$$

with mean values $\mu_2 = -\mu_1 = max\{\Delta_d\} - \Delta_{dmin}$. We validate the upper and lower bounds for hovering displacement in Section VII-E. Unlike GPS errors, the lack of accuracy in the Inertial Measurement Unit (IMU) sensors results in rotational displacement [30]. Thus, in addition to improved UAV linear displacements estimation, our hovering model can also account for rotational displacements $\Delta\theta_r$ (such as yaw, see Fig.1(a)). We first transform rotational $\Delta\theta_r$ into linear displacement Δd_r via $\Delta d = dtan\Delta\theta$ (see Fig.7(b)). Then, we calculate the joint Probability Density Function (PDF) in the linear dimension Δd_T as

$$\begin{aligned} f(\Delta d_T) = \int_{-\infty}^{\infty}\int_{-\infty}^{\infty} f(\Delta d) f(\Delta d_r) \\ \delta_D(\Delta d_T - \Delta d - \Delta d_r) d_{\Delta d_r} d_{\Delta d}, \end{aligned} \tag{16}$$

where $f(\Delta d)$ and $f(\Delta d_r)$ are the PDFs of Δd and Δd_r respectively, and δ_D is the Dirac delta function defined as

$$\delta(\Delta_D d_T) = \begin{cases} 1, & \text{if } \Delta d_T = \Delta d + \Delta d_r \\ 0, & \text{otherwise.} \end{cases} \tag{17}$$

We normalize (16) as

$$f_N(\Delta d_T) = \frac{f(\Delta d_T)}{\int_{-\infty}^{\infty} f(\Delta d_T) d_{\Delta d_T)}}. \tag{18}$$

Note that (16) is needed, since beam misalignment caused by linear displacement (e.g Δd to the left), can be compensated by rotational displacement (e.g $\Delta\theta_r \equiv \Delta d_r$ to the right). Thus, $f_N(\Delta d_T)$ represents the probability density function of $\Delta d_T = \Delta d + \Delta d_r, \forall \Delta d, \Delta d_r$, defined in order to account for possible compensation in the linear dimension.

2) Probability of Blockage and LoS: Based on the Naïve Bayes Classifier described in Section IV-D3, we calculate the probability of blockage P_{block} for a given $\max\{X_{cross}(l_T, l_E)\}$ value as

$$P_{block} = \frac{P(block|\mathcal{D})}{P(block|\mathcal{D}) + P(LoS|\mathcal{D})}. \tag{19}$$

Note that (19) assumes that blockage occurs in isolation. The probability of LoS P_{LoS}, is given by

$$P_{LoS} = 1 - P_{block}. \tag{20}$$

3) Probability of Out of Range: We estimate the probability that the best pair of beams are not evaluated during the beam-sweeping procedure for a UAV-to-Ground link $P_{oR}(UG)$ as

$$P_{oR}(UG) = P(|\ \Delta_d > \widetilde{\Delta d}\ |) = \begin{cases} P(\Delta_d > \widetilde{\Delta d}), & \Delta_d > 0 \\ P(\Delta_d < -\widetilde{\Delta d}), & \Delta_d < 0, \end{cases} \tag{21}$$

where $\widetilde{\Delta d} \in \mathbb{R}^+$ is the estimated lateral displacement covered by half the beam-sweeping angular range $\frac{\theta_r}{2}$ (see Fig.7(b)). We associate $\Delta_d \in \mathbb{R}^-$ to lateral displacement to the left side of the UAV with respect to its forward direction axis, as we show in Fig.7(b), and $\Delta_d \in \mathbb{R}^+$ to lateral displacement to the right side. Considering the mapping between angular displacement range θ_r and lateral displacement $\widetilde{\Delta}_d$, we write (21) as

$$P_{oR}(UG) = P(|\ \Delta_d > (\widetilde{d} \pm \epsilon_T) tan(\frac{\theta_r}{2})\ |). \tag{22}$$

We calculate the out-of-range probability by numerically integrating the PDF of the hovering displacement $f(\Delta_d)$, characterized in Section V-B1 as

$$P_{oR}(UG) = \int_{-\infty}^{\widetilde{-\Delta d}} f(\Delta d) d_{\Delta d} + \int_{\widetilde{\Delta d}}^{\infty} f(\Delta d) d_{\Delta d}), \tag{23}$$

or equivalently,

$$P_{oR}(UG) = 1 - \int_{-\widetilde{\Delta d}}^{\widetilde{\Delta d}} f(\Delta d) d_{\Delta d}. \tag{24}$$

The previous formulation is also applicable to UAV-to-UAV (UU) links. For this, we combine the individual PDF from each UAV $f(\Delta d_{(UAV_1)})$ and $f(\Delta d_{(UAV_2)})$, and estimate the joint PDF $f(\Delta d_C)$ as

$$\begin{aligned} f(\Delta d_C) = \int_{-\infty}^{\infty}\int_{-\infty}^{\infty} f(\Delta d_{(UAV_1)}) f(\Delta d_{(UAV_2)}) \\ \delta_D(\Delta d_C - \Delta d_{(UAV_1)} - \Delta d_{(UAV_2)}) d_{\Delta d_{(UAV_2)}} d_{\Delta d_{(UAV_1)}}. \end{aligned} \tag{25}$$

This calculation is equivalent to (16)-(18). With this approach, we reduce the UAV-to-UAV case to an equivalent UAV-to-Ground link, where one of the UAVs is seen as static, and the second UAV motion is given by the joint PDF in (25), with maximum displacement range $max\{\Delta d_C\} = max\{\Delta d_{(UAV_1)}\} + max\{\Delta d_{(UAV_2)}\}$. Notice that the product in (25) assumes independent hovering motion between UAV transmitter and receiver. We support this assumption with the insights learnt from our experiments, where we compared the behaviour between co-located and separated GPS receivers, and observed how distance decorrelates rapid fluctuations on GPS signals (and consequently, motion during hovering for separated UAVs).

4) Probability of Insufficient Beamwidth: The probability of insufficient beamwidth P_{iB} for certain hovering conditions can be estimated from (21), with $\widetilde{\Delta d}$ the estimated lateral displacement covered by half the beamwidth $\frac{\theta_{3dB}}{2}$.

VI. Algorithm for Overcoming Link Degradation

In this section, we formally describe the algorithm that takes the most appropriate action(s) for (i) establishing a robust communication link right after UAV deployment in a previously unexplored area (Fig.8), and (ii) re-establishing performance levels in an active link that experiences a sudden power drop (Fig.9). We leverage the theoretical path loss estimation introduced in Section III, and well as detection techniques from Sections IV and V. We include pseudo-code for our approach in Algorithms 1 and 2. In addition, we provide a stochastic complexity analysis as well as a discussion on latency and signaling overhead for our solution.

A. Algorithm Description

1) Deployment Stage, (Fig.8, Algorithm 1): Right after UAVs deployment at their targeted GPS coordinates, transmitter and receiver perform beam-sweeping, select the best pair of beams for communication $p_{ms} = (ms_{tx}, ms_{rx})$ and generate the angular distribution of the experimental path loss l_E.

We detect sub-optimum link performance if the loss for the selected pair of beams $l_E(\theta_{ms_{tx}}, \theta_{ms_{rx}})$ is not within the range of expected values given by our theoretical estimation $l_T(\theta_{bs_{tx}}, \theta_{bs_{rx}})$, calculated according to (5). In this case, we calculate the $\max\{X_{cross}(l_T, l_E)\}$ value and estimate the probability of LoS from (19) and (20). From this value, we determine whether our solution can help boost link performance and should be triggered, according to Section V-A. If not, we maintain the current link without any further computations. In affirmative case, we estimate P_{oR} (Section V-B3), according to (21)-(25). We recall that the value of P_{oR} considers both UAV hovering models, as well as the beam-sweeping angular range θ_r. Thus, from its value, we determine the probability that low link performance is due to the best pair of beams being out of range, given current flying conditions and beamforming parameters.

If P_{oR} differs from zero, we check whether the best pair of beams was not evaluated during beam-sweeping, from the $\nabla l_E(\bar{\theta}_{m_{tx}}), \nabla l_E(\bar{\theta}_{m_{rx}})$ values ((7) in Section IV-C), in which case, the UAV is rotated according to Table I. If after rotation, the link is re-established, we add the $\max\{X_{cross}(l_T, l_E)\}$ value labelled as 'LoS' to the ML dataset of observations $\mathcal{D}$. If the link is not re-established, or if $P_{oR} \sim 0$, we move one or both UAVs to achieve LoS conditions. If after motion, link performance is re-established and $P_{oR} \sim 0$, we confirm that blockage was the cause for low link performance, and we add the $\max\{X_{cross}(l_T, l_E)\}$ value labelled as 'block' to $\mathcal{D}$.

Finally, and with independence of the angular range θ_r and resolution δ utilized during beam-sweeping, we calculate the Inverse of the Cumulative Distributive Function (ICDF) of P_{iB} (Section V-B4), and adjust the beamwidth θ_{3dB} to cover the maximum displacement range Δ_d under moderate hovering conditions to achieve $P_{iB} \sim 0$.

2) Operation Stage (Fig.9, Algorithm 2): In operation stage, (see Fig.9), we assume a high performance link was established prior to power drop. Thus, we associate performance degradation to blockage, misalignment loss or a combination of both.

Based on our experimental observations, hovering causes large misalignment loss in aerial links. Thus, we initially assume low performance is due to an underestimation of the hovering conditions. We increase θ_{3dB} (V-B4) to cover Δ_d under strong hovering conditions, according to the hovering model provided in Section V-B1 and values given in Table IV. This approach potentially allows to re-establish link performance without triggering a new beam-sweeping and

Algorithm 1 Deployment Stage

Input: $\widetilde{d} \leftarrow$ GPS location data.
Input: Experimental path loss distribution $l_E \leftarrow$ beam-sweeping.
Input: Selected beams pair $p_{ms} = (ms_{tx}, ms_{rx}) \leftarrow$ beam-sweeping
Input: Evaluated angular range $\theta_R \leftarrow$ beam-sweeping
Input: Theoretical path loss estimation range $l_T(\widetilde{d} \pm \epsilon_T) \leftarrow$ (5).
Input: Dataset of observations $\mathcal{D}$
Output: Beamwidth θ_{3dB} and set of UAV required actions.

```
1. Check for reduced link performance.
2.  if l_E(θ_{ms_tx}, θ_{ms_rx}) ∉ l_T(θ_{ns_tx}, θ_{ns_rx}),
3.      Determine whether to trigger solution.
4.      Calculate max{X_cross(l_T, l_E)} ← (9).
5.      Obtain P(LoS|D), P(block|D)
6.      max{X_cross}, (10), Fig.11.
7.      Determine whether LoS conditions.
8.      if P(LoS|D) < P(block|D) ← (11),
9.          Estimate P_oR(θ_R) ← Section V-B3.
10.         if P_oR ≠ 0,
11.             calculate | ∇l_{E(θ̄_{m_tx})} |, | ∇l_{E(θ̄_{m_rx})} |← (10).
12.             if | ∇l_{E(θ̄_m)} |< ξ_th,
13.                 Label max{X_cross}as LoS.
14.             else
15.                 Rotate transmitter and/or receiver ← Table I.
16.                 if l_E(θ_{ms_tx}, θ_{ms_rx}) ∈ l_T(θ_{ns_tx}, θ_{ns_rx}),
17.                     Label max{X_cross}as LoS.
18.                 else
19.                     Assume blockage and laterally move UAVs.
20.                     Label max{X_cross}as blockage.
21.                 end
22.             end
23.         end
24.     end
25. end
26. return θ_{3dB} for moderate hovering← Section V-B4, Table IV.
```

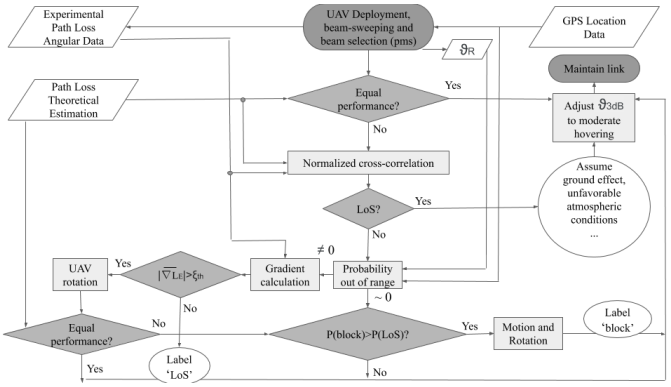

Fig. 8: Algorithm for robust links during deployment.

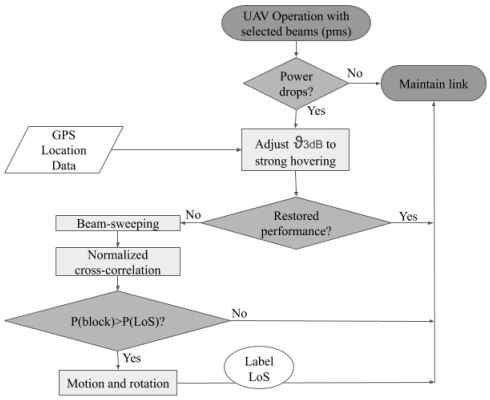

Fig. 9: Algorithm for robust links during operation.

Algorithm 2 Operation Stage

Input: $\widetilde{d} \leftarrow$ GPS location data.
Input: $l_{E_{ref}}(ms_{tx}, ms_{rx})$ after beam alignment.
Input: Current $l_E(ms_{tx}, ms_{rx})$.
Output: Beamwidth θ_{3dB} and set of UAV required actions.
1. Check for power drop.
2. **if** $l_E(\theta_{ms_{tx}}, \theta_{ms_{rx}}) \neq l_{E_{ref}}(ms_{tx}, ms_{rx})$
3. **return** θ_{3dB} for strong hovering$\leftarrow$ Section V-B4, Table IV.
4. **end**
5. Check for restored link.
6. **if** $l_E(\theta_{ms_{tx}}, \theta_{ms_{rx}}) \neq l_{E_{ref}}(ms_{tx}, ms_{rx})$
7. Trigger new beam-sweeping.
8. Calculate $\max\{X_{cross}(l_T, l_E)\} \leftarrow$ (9).
9. Obtain $P(LoS|\mathcal{D}), P(block|\mathcal{D}) \leftarrow$
10. $\max\{X_{cross}\}, (10), Fig.11.$
11. Determine whether LoS conditions
12. **if** $P(LoS|\mathcal{D}) < P(block|\mathcal{D}) \leftarrow$ (11),
13. Assume blockage and laterally move UAVs.
14. Label $\max\{X_{cross}\}$as blockage.
15. **end**
16. **end**

interrupting communication. If the link is not re-established, we trigger beam-sweeping l_E, and run the obstacle detection method, similarly to deployment stage, following the theoretical analysis given in Section V-B2.

B. Algorithm Complexity Analysis

The algorithm steps with higher complexity order as follow:

- $\max\{X_{cross}(l_T, l_E)\}$ achievable with $\mathcal{O}(M_{tx} \cdot M_{rx})$ [25].
- P_{oR} with complexity $\mathcal{O}(\rho - 1) \sim \mathcal{O}(\rho)$, with $\rho - 1$ additions and products, and ρ the dimension of the discrete function to be integrated (numerical resolution), and ICDF(P_{iB}) with complexity $\sim \mathcal{O}(\rho + 2\rho log(\rho))$, as sorting is required.
- $\nabla l_E(\theta_{m_{tx}}), \nabla l_E(\theta_{m_{rx}})$ with complexity of $\sim \mathcal{O}(M_{tx} \cdot M_{rx})$ as it requires $2M_{tx}(M_{rx} - 1) + 2M_{rx}(M_{tx} - 1)$ subtractions and $M_{tx}(M_{rx} - 1) + M_{rx}(M_{tx} - 1)$ divisions and additions.
- l_T with complexity $\mathcal{O}(\widetilde{N_{tx} \cdot N_{rx}})$, with last three terms in (5) computed offline, and $\widetilde{FSPL}$ calculated once, and added to all $P_N = N_{tx} \cdot N_{rx}$ pair of beams.
- Beam-sweeping procedure with $\mathcal{O}(M_{tx} \cdot M_{rx})$.

Table V summarizes this computation complexity. In Table VI, we show the required computations for the link to be reestablished in a probabilistic manner. From Table VI, notice that by leveraging our stochastic analysis in Section V-B, we reduce the number of high complexity computations required to identify the cause for low performance in the deployment stage. Moreover, in the operation stage, we reduce the complexity required to reestablish the link (from quadratic to logarithmic), avoiding to trigger a new beam-sweeping with probability $P_{LoS}P_{iB}$.

TABLE V: Complexity Analysis

Reference	Computation	Complexity
(i)	$\max\{X_{cross}(l_T, l_E)\}$, (9)	$\mathcal{O}(M_{tx} \cdot M_{rx})$ [25]
(ii)	P_{oR}, (24)	$\mathcal{O}(\rho)$
(iii)	$ICDF(P_{iB})$, Sec. V-B4	$\mathcal{O}(\rho + 2\rho log(\rho))$
(iv)	$\nabla l_E(\theta_{m_{tx}}), \nabla l_E(\theta_{m_{rx}})$, (7)	$\mathcal{O}(M_{tx} \cdot M_{rx})$
(v)	l_T, (5)	$\mathcal{O}(N_{tx} \cdot N_{rx})$
(vi)	Beam-sweeping	$\mathcal{O}(M_{tx} \cdot M_{rx})$

C. Discussion on Algorithm Latency and Signaling Overhead

In the standard solution, a potential sub-optimal pair of beams remains fixed after beam-selection. In contrast, our approach help establish or recover high throughput links. To achieve this, we use the Robot Operating System (ROS) framework to establish communication between UAVs, as well as between on-board sensors and the UAV's own computing module (NVIDIA Jetson TX2). Through ROS-based messaging, both UAVs perform synchronized and coordinated motion in a distributed manner. Specifically, ROS follows a publish-subscribe model to communicate the UAV sources that generate (and *publish* data), and the UAV ends that retrieve this data (by *subscribing* to that *topic*). The 3-dB beamwidth and motion directives estimated at the UAV receiver are published on ROS *topics* called *3-dB Elevation Beamwidth* and *motion directives*. The transmitter UAV subscribes to these topics and reads the angular rotation and 3-dB beamwidth commands. Then, both transmitter and receiver use their IMU, GPS and mmWave sensors together with the received commands to achieve the desired coordinated motion and 3-dB beamwidth adjustment.

From our experimental findings, localised ROS messaging within a UAV typically introduces a latency below 1 ms, less than the inter-UAV ROS messaging delay of $\approx$ 5 ms. Given the low complexity of our algorithmic solution presented in Section VI-B, the delay caused by calculations performed on top of the standard beam-sweeping approach is

TABLE VI: Stochastic Computational Analysis

Stage	Probability	Condition	Computations (from Table V)
Deployment	P_{LoS}	$P_{LoS} > P_{block}$	(i),(iii),(v)
Deployment	$P_{block}(1-P_{oR})$	$P_{LoS} < P_{block}$ and $P_{oR} \sim 0$	(i),(ii),(iii),(v)
Deployment	$P_{block}P_{oR}$	$P_{LoS} < P_{block}$ and $P_{oR} \neq 0$	(i),(ii),(iii),(iv),(v)
Operation	$P_{LoS}P_{iB}$	$P_{LoS} > P_{block}$ and $P_{iB} \neq 0$	(iii)
Operation	$P_{block}P_{iB}+$ $(1-P_{iB})$	$(P_{LoS} < P_{block}$ and $P_{iB} \neq 0)$ or $(P_{iB} \sim 0)$	(i),(iii),(v),(vi)

upper bounded by 10 ms. Thus, UAV mechanical steering, which takes at most 100-200 ms for angular rotation below 10°, is the highest contributor to latency. Even though our solution takes additional time (upper bounded by hundreds of ms), during this time the link is not disrupted, but rather gradually enhanced as the UAVs rotate or change location. Moreover, given the long time-span of hovering, UAVs are not expected to significantly change location within several seconds. Therefore, the throughput achieved with our solution, even delay before converging on the best beam alignment, is always higher compared with the standard.

Regarding the overhead introduced by the use of ROS, only the 3-dB beamwidth (float number) and the motion direction (integer number, 1: right, 0: left) are shared though ROS topics on a wireless WiFi channel. These, along with their headers (timestamp, sequence number and frame), require less than 50 bps.

VII. Results and Performance Evaluation

In this Section, we evaluate the performance for the algorithm presented in Section VI. To this extent, we first present the experimental set-up in VII-A, and classify collected data according to their temporal scale in VII-B. In VII-D and VII-C we show results for each individual detection technique proposed in Section IV. Then, in VII-E, we validate the hovering model introduced in Section V-B1, and present results for the stochastic analysis used for complexity reduction. We evaluate the algorithm performance in Section VII-F.

A. Experimental Set-up

To run our experiments, we mount a Terragraph mmWave channel sounder on each of the two DJI M600 UAVs used to setup a UAV-to-UAV link. Each UAV can carry up to 15.5 Kg, and the total payload weight including six batteries, channel sounder unit and the mounting hardware is close to 14 Kg. This gives an effective flight time of 10-12 minutes.

The channel sounders operate the WiFi 802.11ad standard, allowing us to perform beam-sweeping and beam-selection during flight to find the best pair of beams for communication. Both channel sounders are connected to a central computer through an Ethernet switch, to synchronize transmissions and log measurements at the receiver. The chosen channel is centered at 60.48 GHz and has a bandwidth of 2.16 GHz.

Terragraph channel sounders perform only azimuth steering. To ensure high received signal power, we select the narrowest possible beamwidth θ_{3dB} of 2.8°, unless otherwise specified. For all experiments, we maintain a distance of 6 meters between transmitter and receiver.

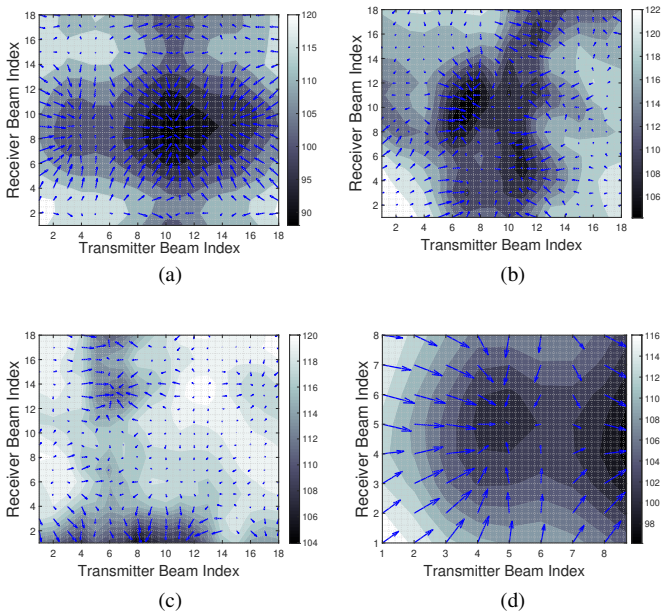

Fig. 10: Minus gradient direction on measured angular data (a) reference data for threshold setting, (b) not out of range, centroid (main beam) within evaluated range (c) out of range (d) out of range, centroid is a secondary side lobe.

B. Relative Time Scales Magnitude

The time scale magnitude refers to the complete time-span the radios take to perform beam-sweeping and collect l_E. In the WiFi standard 802.11ad, this process can take from hundreds of ms up to a few seconds to complete [11]. During such time, transmitter, receiver and obstacle change of location is negligible, given the long time-span effect of hovering. We denote this condition as Small Temporal Scale (STS). We however, chose to extend the algorithm evaluation to a more general case, in which transmitter, receiver, and obstacle locations may randomly vary during the beam-sweeping time and within the hovering maximum displacement range. We denote these conditions as Large Temporal Scale (LTS).

To evaluate our work performance under LTS, we operate beam-sweeping with a time-span of 2 minutes, in which different subsets within the angular beam-sweeping range θ_r are evaluated every few seconds. Under these conditions, l_E is perturbed, as hovering UAVs change location during data collection. We demonstrate that, even under these conditions, our algorithm is still capable of determining the cause of loss with high accuracy.

C. Out of Range Detection Performance

In this Section, we show the performance for the out of range detection technique proposed in Section IV-C. We first determine the threshold values $\xi_{th(tx)}, \xi_{th(rx)}$ using l_E in Fig.2(d), as reference (offline characterization). The threshold

TABLE VII: Out of Range Performance

l_E	Condition	Required rotation
10(b)	$\mid \nabla \bar{l}_{E(\theta_{m_{tx}})} \mid = \mid -0.048 \mid < 0.98$	Transmitter: none
	$\mid \nabla \bar{l}_{E(\theta_{m_{rx}})} \mid = \mid 0.107 \mid < 0.39$	Receiver: none
10(c)	$\mid \nabla \bar{l}_{E(\theta_{m_{tx}})} \mid = \mid -0.057 \mid < 0.98$	Transmitter: none
	$\mid \nabla \bar{l}_{E(\theta_{m_{rx}})} \mid = \mid -0.56 \mid > 0.39$	Receiver to $-\hat{\theta_{m_{rx}}}$
10(d)	$\mid \nabla \bar{l}_{E(\theta_{m_{tx}})} \mid = \mid 2.39 \mid > 0.98$	Transmitter to $+\hat{\theta_{m_{tx}}}$
	$\mid \nabla \bar{l}_{E(\theta_{m_{rx}})} \mid = \mid 0.37 \mid < 0.39$	Receiver: none

values are set as x10 (>> criteria) the obtained values $\nabla \bar{l}_{E(\theta_{m_{tx}})}, \nabla \bar{l}_{E(\theta_{m_{rx}})}$ from (7).

Fig.10(a), shows the result of the gradient calculation for the reference scenario in Fig.2(d), where the arrows point towards the centroid, in the $-\nabla l_E$ direction (direction of greatest path loss decrease). Notice that, as the centroid is located towards the middle of l_E, the averaged value of $-\nabla l_E$ over all pair of beams, is ~ 0.

To evaluate the method performance, we show results for UAV-to-UAV experimental data. In Fig.10 (b) we show a case where the centroid is within the angular range evaluated during beam-sweeping, thus, contained in l_E. In contrast, in Fig.10(c) the centroid is out of the beam-sweeping angular range. Table VII shows the required actions for both cases according to Table I. For the former case, no rotation is required, whereas for the latter, rotation of the receiver towards its negative angular direction is needed. We can observe from Figs.10(b) and (c) that our proposed actions match both situations.

To further evaluate the algorithm, we present a more complex case in Fig.10 (d), where the centroid is located towards the middle of l_E, but corresponds to the antenna secondary side lobe thus, providing sub-optimal performance. Our results in Table VII prove that, even in this scenario, our method still detects the required rotation for the transmitter, when sufficient angular information is contained in l_E.

D. Obstacle Detection Performance

In this Section, we show the performance for the obstacle detection technique introduced in Section IV-D3. To create the dataset of observations $\mathcal{D}$, we use experimental data collected over multiple scenarios l_E, including open areas, rich multipath environments, presence and absence of blockage, and small and large time scale conditions. From these data, and our theoretical estimation l_T (Section III), we calculate the $\max\{X_{cross}(l_T, l_E)\}$ value from (9). The labelled values for all scenarios are represented in Fig.11, which we use to build the decision boundaries of the Naïve Bayes classifier. In Table VIII, we show the classification decision for each scenario, given by (11), along with its confidence ratio defined in (19) and (20). From these results, we successfully detect the presence and absence of blockage with high confidence for most of the scenarios considered.

In order to show a limitation of the proposed detection method, we include a case where the detection method fails in Table VIII. In this case, a static human blocked the whole angular range θ_r, equally attenuating all angular directions. Given the lack of diversity in the angular domain, our proposed solution fails, according to the definition given in (9). Despite this, our algorithm as defined in Figs.8 and 9 prevents from adding this data to $\mathcal{D}$, as new data is added only when taking an action leads to link performance enhancement.

TABLE VIII: Obstacle Detection Performance

Scenario	Time Scale	True label	max $\{X_{cross}\}$	Naïve Bayes Classifier (Confidence)
Parking Lot	STS	'LoS'	0.812	'LoS'(99.92%)
Grassland	STS	'LoS'	0.808	'LoS'(99.9%)
Rich Multipath	LTS	'block'	0.502	'block'(99.14%)
	STS	'LoS'	0.693	'LoS' (77.07%)
	STS	'block'	0.73	'LoS' (94.2%)
UAV Arena	LTS	'block',M100	0.6	'block' (90.39%)
	LTS	'block',M100	0.574	'block' (95.31%)
	LTS	'block',M100	0.638	'block' (72.41%)
	LTS	'block',M100	0.655	'block' (58%)
	LTS	'block',Pillar	0.601	'block' (90%)
	LTS	'LoS'	0.677	'LoS' (62.77%)
	LTS	'LoS'	0.691	'LoS' (75.6%)

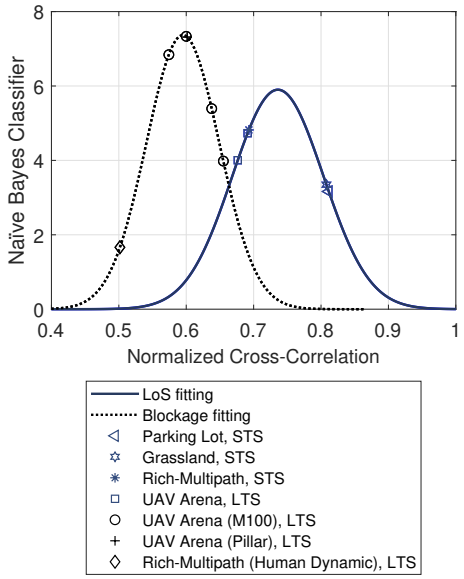

Fig. 11: Labelled values of $\max\{X_{cross}(l_T, l_E)\}$ for different scenarios used in Naïve Bayes classifier for obstacle detection.

E. Hovering Model Validation and Stochastic Approach

In order to present results for the stochastic analytical approach presented in Section V-B, we estimate the probability of out of range P_{oR} given by (24). In Fig.12(a) we show the ICDF(P_{oR}) for UAV-to-Ground links, and Δ_d selected for moderate hovering conditions according to Table IV. For the term $f(\Delta d)$ in (24), we utilize the Gaussian and bi-modal hovering models given by (12) and (13). Moreover, since for the bi-modal case, the two modes mean values within $f(\Delta d)$ are unpredictable, we run a 100 iteration Monte Carlo simulation in which we randomly select their values, and adjust each mode variance in order to cover $\max\{\Delta_d\}$. We then calculate the averaged P_{oR} over all iterations.

In order to determine which model -Gaussian or bi-modal- performs better, we compare their performance with the P_{oR} calculated using as $f(\Delta d)$ the experimental hovering distribution characterized from collected RTK-GPS data, shown in

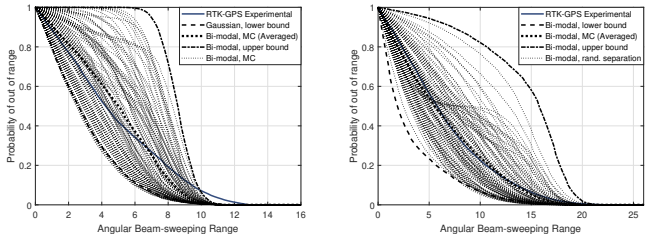

(a) (b)

Fig. 12: Estimated $P_{oR}(\theta_r)$ for moderate hovering conditions, $d = 6$ m, and (a) UAV-to-Ground links (b) UAV-to-UAV links.

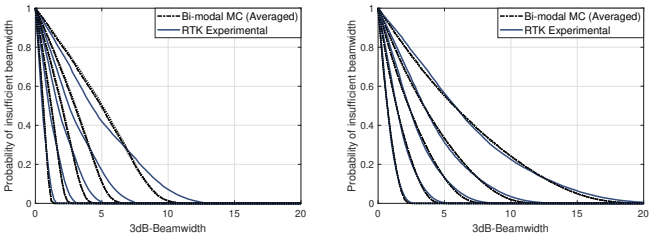

(a) (b)

Fig. 13: $P_{iB}(\theta_{3dB}, d)$ for (a) UAV-to-Ground and (b) UAV-to-UAV links, d (m) = {50, 25, 15, 10, 6} from left to right.

Fig.7(a). From Fig.12(a), we observe that the bi-modal distribution best fits experimental data. Additionally, we validate the upper and lower bounds for the bi-modal distribution given in (14) and (15). Fig.12(b) shows equivalent results for UAV-to-UAV links, where $f(\Delta d)$ in (24) is obtained from the joint PDF for both UAVs, after normalizing (25).

This stochastic analysis can be used as a proactive technique to adjust θ_r to expected hovering prior to deployment, and minimize P_{oR}. However, we choose not to constraint the system to use a specific θ_r, and instead, detect out of range for any given value, making our approach compatible with other existing works θ_r reduction.

In Fig.13, we present similar results for the ICDF(P_{iB}) and multiple distances between transmitter and receiver. From this analysis, we determine the required θ_{3dB} to prevent misalignment loss with certain targeted probability, for a given distance, type of link and hovering conditions. In Table IX, we provide the required θ_{3dB} for $P_{iB} < 5\%$, for multiple conditions, including strong hovering, according to Table IV.

For UAV-to-UAV links, the required θ_{3dB} significantly grows compared to UAV-to-Ground links, to guarantee sufficient coverage when transmitter and receiver UAVs hover in opposite directions.

F. Algorithm Performance

We evaluate the performance of our proposed algorithm in Section VI, on the UAV-to-UAV link in Fig.14, where the LoS is blocked by the presence of a M100 UAV. Both UAVs rely on GPS for localization, and we characterize their hovering as a bi-modal distribution. We utilize an angular subset $l_E \in \mathbb{R}^{9x9}$ with $\theta_r = 11.2°$ of the data shown in Fig.2(b), leaving the centroid out of the subset. By doing so, we evaluate the

TABLE IX: Required θ_{3dB} such that $P_{iB} < 0.05$ for different, distance, type of links and hovering conditions

d (m)	$\boldsymbol{\theta_{3dB}(UG)}$ **Moderate Hovering**	$\boldsymbol{\theta_{3dB}(UG)}$ **Strong Hovering**	$\boldsymbol{\theta_{3dB}(UU)}$ **Moderate Hovering**	$\boldsymbol{\theta_{3dB}(UU)}$ **Strong Hovering**
50	1.1°	3°	1.8°	5.1°
25	*2.2°*	6°	*3.6°*	10.2°
15	*3.6°*	10°	*6°*	16.9°
10	*5.4°*	15°	*9°*	25°
6	*9.1°*	24.6°	*15°*	40.6°

algorithm performance in a situation wherein, in addition to blockage, the angular directions containing high performing beams are not evaluated during beam-sweeping. We take the centroid performance in Fig.2(b), as well as in Fig.2(a) (same scenario under LoS), as baselines for evaluation. We consider the deployment stage in Section VI-A1, so that a high performance link has not previously been established.

Following Fig.8, we first prove the link sub-optimal performance, as the path loss for the selected pair of beams after beam-sweeping (lowest path loss in the subset), is not within the theoretical estimated range according to (5) $l_E(\theta_{ms_{tx}}, \theta_{ms_{rx}}) = 96.56dB \notin [88.73dB, 92.25dB]$. We select a value of $\epsilon_T = 1.2m$ for the theoretical estimation, in order to consider the maximum joint displacement range for simultaneous hovering from two UAVs under moderate hovering conditions, and characterize $2L_{Afr} \sim 7dB$ offline.

To determine whether our solution should be triggered, from Fig.11 and the $\max\{X_{cross}(l_T, l_E)\} = 0.381$ value, we calculate $P(LoS|\mathcal{D}) = 6.32 \cdot 10^{-6}, P(block|\mathcal{D}) = 2.7610^{-3}$ according to (10). We determine not to be under LoS conditions (11). To select what effect we should tackle first, we estimate $P_{oR}(\theta_R = 11.2°) = 77.62\%$ for the worst hovering pattern (upper bound in Fig.12(b)), and our system parameters. Given that $P_{oR} \neq 0$, we calculate the averaged gradient over the filtered subset l_E according to (7). We show this result in Fig.15(a). After averaging the gradient projection over the transmitter and receiver angular pointing directions, we obtain $| \bar{E(\theta_{m_{tx}})} | = | -0.12 | < 0.98, | \bar{\nabla l_{E(\theta_{m_{rx}})}} | = | 0.7 | > 0.39$, and thus, only receiver is rotated towards $+\hat{\theta_{m_{rx}}}$ (see Table I). After rotation, the centroid is within the coverage range, and the path loss is reduced to 95.18 dB (a factor of 27.22%). Since, even after rotation, the link performance is not within the estimated path loss range, link degradation is associated to blockage with a certainty of 99.81%, according to (19)-(20). After UAVs displacement to overcome blockage, path loss decreases an additional factor of 64.6%, according to Fig.2(a).

To show the PHY-bitrate gain achievable after overcoming the obstacle, we run the experiment in Fig.14, during which we continuously log the PHY-bitrate under blockage conditions. After half the flying time, we move the M100 blocking UAV and continue measurements on the link under LoS conditions. We show the Empirical Cumulative Distribution Function (ECDF) for the PHY-bitrate in presence and absence of blockage in Fig.15(b). The M100 introduces an average of 6.67 dB additional path loss, which translates into a fall in the bitrate of 1.45 Gbps. Finally, we fix the beamwidth $\theta_{3dB} = 15°$ according to Table IX, to maintain $P_{iB} < 95\%$.

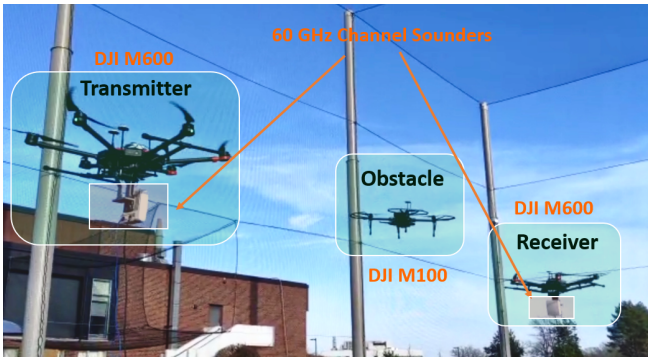

Fig. 14: UAV-to-UAV 60 GHz link under blockage conditions.

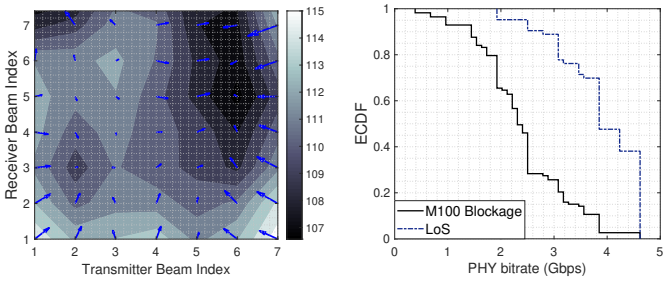

(a) (b)

Fig. 15: (a) Averaged gradient over l_E for out of range detection. (b) Effect of a M100 UAV blockage on PHY-bitrate.

VIII. Conclusions

In this paper, we characterize the impact of factors that significantly affect UAV communications in the 60 GHz mmWave band, specifically blockage and those arising from the continuous UAV hovering motion. Based on our observations on experimental data collected with channel sounders mounted on M600 DJI UAVs during the standard beam-sweeping procedure, we propose to exploit the information contained in the angular domain to identify the cause(s) for link performance degradation. We take a stochastic analytical approach which, combined with individual solutions to the effects considered, help identify the cause for sub-optimal link performance while avoiding unnecessary computations. Our individual solutions involve feature tracking from image processing as well supervised ML classification. Moreover, with our stochastic approach, we create a UAV hovering bi-modal characterization for given hovering conditions during flight and beamforming configuration. Using empirical data, we demonstrate its superior accuracy compared to simple Gaussian existing models. Our proposed algorithm is validated with experimental data, and reduces link loss a factor up to 74.7%. This translates into 260% PHY-bit-rate gain compared to the classical standards-defined approach.

Acknowledgement

This work is supported by the Office of Naval Research under grant N000141612651. The Terragraph Channel Sounders used for the experiments in this paper are part of the Facebook Connectivity initiative.

References

[1] J. Zhao, F. Gao, G. Ding, T. Zhang, W. Jia, and A. Nallanathan, "Integrating communications and control for UAV systems: Opportunities and challenges," *IEEE Access*, vol. 6, pp. 67519–67527, 2018.

[2] Z. Xiao, P. Xia, and X.-G. Xia, "Enabling UAV cellular with millimeter-wave communication: Potentials and approaches," *IEEE Communications Magazine*, vol. 54, no. 5, pp. 66–73, 2016.

[3] T. Nitsche, A. B. Flores, E. W. Knightly, and J. Widmer, "Steering with eyes closed: mm-wave beam steering without in-band measurement," in *IEEE Conference on Computer Communications (INFOCOM)*, pp. 2416–2424, 2015.

[4] M. Hashemi, A. Sabharwal, C. E. Koksal, and N. B. Shroff, "Efficient beam alignment in millimeter wave systems using contextual bandits," in *IEEE Conference on Computer Communications (INFOCOM)*, pp. 2393–2401, 2018.

[5] M. Gapeyenko, V. Petrov, D. Moltchanov, S. Andreev, N. Himayat, and Y. Koucheryavy, "Flexible and reliable UAV-assisted backhaul operation in 5G mmWave cellular networks," *IEEE Journal on Selected Areas in Communications*, vol. 36, no. 11, pp. 2486–2496, 2018.

[6] J. Zhao and W. Jia, "Channel transmission strategy for mmWave hybrid UAV communications with blockage," *Electronics Letters*, vol. 54, no. 2, pp. 74–76, 2017.

[7] L. Zhang, H. Zhao, S. Hou, Z. Zhao, H. Xu, X. Wu, Q. Wu, and R. Zhang, "A survey on 5G millimeter wave communications for UAV-assisted wireless networks," *IEEE Access*, vol. 7, pp. 117460–117504, 2019.

[8] M. Mozaffari, W. Saad, M. Bennis, and M. Debbah, "Mobile unmanned aerial vehicles (UAVs) for energy-efficient Internet of Things communications," *IEEE Transactions on Wireless Communications*, vol. 16, no. 11, pp. 7574–7589, 2017.

[9] S. Zhang, H. Zhang, Q. He, K. Bian, and L. Song, "Joint trajectory and power optimization for UAV relay networks," *IEEE Communications Letters*, vol. 22, no. 1, pp. 161–164, 2017.

[10] M. Zarifneshat, C.-J. Liu, and L. Xiao, "A Protocol for Link Blockage Mitigation in mm-Wave Networks," in *IEEE 14th International Conference on Mobile Ad Hoc and Sensor Systems (MASS)*, pp. 215–223, 2017.

[11] Y. Yaman and P. Spasojevic, "Reducing the LOS ray beamforming setup time for IEEE 802.11 ad and IEEE 802.15. 3c," in *IEEE MILCOM*, pp. 448–453, 2016.

[12] M. Zarifneshat, L. Xiao, and J. Tang, "Learning-based Blockage Prediction for Robust Links in Dynamic Millimeter Wave Networks," in *16th Annual IEEE International Conference on Sensing, Communication, and Networking (SECON)*, pp. 1–9, 2019.

[13] M. Park and Y. Choi, "Performance analysis of degradation detection method on millimeter wave channel," in *IEEE International Conference on Information and Communication Technology Convergence (ICTC)*, pp. 971–973, 2015.

[14] M. Giordani, M. Mezzavilla, A. Dhananjay, S. Rangan, and M. Zorzi, "Channel dynamics and SNR tracking in millimeter wave cellular systems," in *European Wireless; 22th European Wireless Conference*, pp. 1–8, VDE, 2016.

[15] S. Sur, X. Zhang, P. Ramanathan, and R. Chandra, "BeamSpy: enabling robust 60 GHz links under blockage," in *13th {USENIX} Symposium on Networked Systems Design and Implementation ({NSDI} 16)*, pp. 193–206, 2016.

[16] Y. Koda, K. Yamamoto, T. Nishio, and M. Morikura, "Reinforcement learning based predictive handover for pedestrian-aware mmWave networks," in *IEEE Conference on Computer Communications Workshops (INFOCOM WKSHPS)*, pp. 692–697, 2018.

[17] V. Petrov, M. Komarov, D. Moltchanov, J. M. Jornet, and Y. Koucheryavy, "Interference and SINR in millimeter wave and terahertz communication systems with blocking and directional antennas," *IEEE Transactions on Wireless Communications*, vol. 16, no. 3, pp. 1791–1808, 2017.

[18] N. Tafintsev, D. Moltchanov, M. Gerasimenko, M. Gapeyenko, J. Zhu, S.-p. Yeh, N. Himayat, S. Andreev, Y. Koucheryavy, and M. Valkama, "Aerial Access and Backhaul in mmWave B5G Systems: Performance Dynamics and Optimization," *IEEE Communications Magazine*, vol. 58, no. 2, pp. 93–99, 2020.

[19] L. Zhu, J. Zhang, Z. Xiao, X. Cao, X.-G. Xia, and R. Schober, "Millimeter-Wave Full-Duplex UAV Relay: Joint Positioning, Beamforming, and Power Control," *arXiv preprint arXiv:2004.11070*, 2020.

[20] L. Zhu, J. Zhang, Z. Xiao, X. Cao, D. O. Wu, and X.-G. Xia, "3-D beamforming for flexible coverage in millimeter-wave UAV communi-

cations," *IEEE Wireless Communications Letters*, vol. 8, no. 3, pp. 837–840, 2019.
[21] S. Huang, Y. Gao, W. Xu, Y. Gao, and Z. Feng, "Energy-angle domain initial access and beam tracking in millimeter wave V2X communications," *IEEE Access*, vol. 7, pp. 9340–9350, 2019.
[22] Y. Ke, H. Gao, W. Xu, L. Li, L. Guo, and Z. Feng, "Position prediction based fast beam tracking scheme for multi-user uav-mmwave communications," in *IEEE International Conference on Communications (ICC)*, pp. 1–7, 2019.
[23] C. A. Balanis, *Antenna theory: analysis and design*. John wiley & sons, 2016.
[24] W. Hong, K.-H. Baek, Y. Lee, Y. Kim, and S.-T. Ko, "Study and prototyping of practically large-scale mmWave antenna systems for 5G cellular devices," *IEEE Communications Magazine*, vol. 52, no. 9, pp. 63–69, 2014.
[25] J.-C. Yoo and T. H. Han, "Fast normalized cross-correlation," *Circuits, systems and signal processing*, vol. 28, no. 6, p. 819, 2009.
[26] "MATRICE 600 UAV Specifications." https://www.dji.com/es/matrice600/info. Accessed: 2020-04-01.
[27] M. T. Dabiri, H. Safi, S. Parsaeefard, and W. Saad, "Analytical channel models for millimeter wave UAV networks under hovering fluctuations," *IEEE Transactions on Wireless Communications*, 2020.
[28] D. R. Fuhrmann, J. Stomberg, S. Nooshabadi, D. McIntire, and W. Merill, "Node Synchronization in a Wireless Sensor Network Using Unreliable GPS Signals," in *IEEE Military Communications Conference*, pp. 630–636, 2014.
[29] T.-c. Li, J.-y. Su, W. Liu, and J. M. Corchado, "Approximate Gaussian conjugacy: parametric recursive filtering under nonlinearity, multimodality, uncertainty, and constraint, and beyond," *Frontiers of Information Technology & Electronic Engineering*, vol. 18, no. 12, pp. 1913–1939, 2017.
[30] L. Sahawneh and M. Jarrah, "Development and calibration of low cost MEMS IMU for UAV applications," in *5th International Symposium on Mechatronics and Its Applications*, pp. 1–9, IEEE, 2008.

Sara Garcia Sanchez received the B.S. and M.S. degrees in Electrical Engineering from Universidad Politecnica de Madrid in 2016 and 2018 respectively. She is currently a PhD candidate at the Department of Electrical and Computer Engineering in Northeastern University, under the guidance of Professor Kaushik Roy Chowdhury. Her research interests include mmWave, UAV communications, MIMO and optimization techniques.

Kaushik Roy Chowdhury (M'09-SM'15) received the M.S. degree from the University of Cincinnati in 2006, and the Ph.D. degree from the Georgia Institute of Technology in 2009. He is currently a Professor in the Electrical and Computer Engineering Department. He was a winner of the Presidential Early Career Award for Sci- entists and Engineers (PECASE) in 2017, ONR Director of Research Early Career Award in 2016 and the NSF CAREER Award in 2015. His current research interests include deep learning for wireless sensing and spectrum access, networked robotics, wireless RF energy harvesting/transfer and IoT applications for intra/on-body communication.

TABLE X: TABLE OF NOTATIONS

Symbol	Description
List of Acronyms	
$mmWave$	Millimeter wave
UAV	Unmanned Aerial Vehicle
$PHY-bitrate$	Physical layer bitrate
Tx, Rx	Transmitter, Receiver
$(N)LoS$	(Non-)Line-of-Sight
ML	Machine Learning
SNR	Signal-to-Noise Ratio
$FSPL$	Free Space Path Loss
RF	Radio Frequency
RTK	Real-Time Kinematic
IMU	Inertial Measurement Unit
$ICDF$	Inverse of the Cumulative Distribution Function
$ECDF$	Empirical Cumulative Distribution Function
LTS/STS	Large / Small Temporal Scale
PDF	Probability Density Function
ROS	Robot Operating System
Path Loss Angular Distribution Parameters	
l_E	Experimental path loss angular distribution
l_T	Theoretical path loss angular distribution
m_{tx}, m_{rx}	Beam index for Tx, Rx over l_E
M_{tx}, M_{rx}	Total number of beams for Tx, Rx over l_E
P_M	Number of beam pairs evaluated during beam-sweeping
p_{ms}	Pair of beam fixed after standard beam-selection
N_{tx}, N_{rx}	Total number of beams for Tx, Rx over l_T
P_N	Number of beam pairs included in the estimation l_T
n_{tx}, n_{rx}	Beam index for Tx, Rx over l_T
θ	Azimuth
$\theta_{ns_{tx}}$,$\theta_{ns_{rx}}$	Beam pointing directions for Tx, Rx over l_T
p_{ms}	Best beam pair (lower loss) according to l_T
$\widetilde{d}$	GPS-based measured distance
ϵ_T	GPS error
l_{tx} and l_{rx}	Tx, Rx beam misalignment loss
δ	Beam-sweeping angular resolution
θ_r	Beam-sweeping angular range
ϵ_E	Experimental path loss error
Antenna Parameters	
θ_{3dB}	Antenna half-power beamwidth
θ_{bs}	Antenna broadside angular direction
$f_{tx}(\theta), f_{rx}(\theta)$	Tx, Rx antenna radiation patterns
E_T	Total radiated electric field
E_0	Single element radiated electric field
β	Phase excitation between radiating elements
d_s	Distance between radiating elements
c	Speed of light in vacuum
S	Number of radiating elements in horizontal axis
L_{Afr}	Loss caused by the UAV airframe
f_c	Frequency of operation
Feature Tracking Parameters for Out of Range Detection	
$\xi_{th(tx)}, \xi_{th(rx)}$	Tx, Rx thresholds to perform rotation
d_{l_E,l_T}	Euclidean distance between l_E and l_T
w	Window containing the feature l_T
x_{cross}	Normalized cross-correlation between l_E and l_T
ML Parameters for Obstacle Detection	
$\mathcal{D}$	Dataset of empirical observations
$P(LoS\|\mathcal{D}), P(block\|\mathcal{D})$	Posteriori probability of LoS, blockage
$P(\mathcal{D}\|LoS), P(\mathcal{D}\|block)$	Likelihood function for LoS, blockage
$P(\mathcal{D})$	Evidence given the dataset of observations
P_{LoS},P_{block}	Probability of LoS, blockage
Stochastic Analytical Approach Parameters	
Δ_d	UAV hovering displacement range
μ_1, μ_2	Mean values for bi-modal hovering distribution
σ_1^2, σ_2^2	Variance for bi-modal hovering distribution
v_1, v_2	Bi-modal distribution tailor parameters
$\Delta_{d_{min}}$	Minimum hovering range
Δd_r	Linear hovering displacement
$\Delta\theta_r$	Rotational hovering displacement
Δd_T	Joint displacement in the linear dimension
$f(\Delta d)$	PFD for hovering displacement Δd
Δ_D	Dirac delta function
$f_N(\Delta d_T)$	Normalized Δd_T
$\widetilde{\Delta d}$	Estimated hovering displacement for $\frac{\theta_r}{2}$
P_{oR}	Probability for out of range
Δd_C	Joint displacement for UAV-UAV links
P_{iB}	Probability for insufficient beamwidth
ρ	Numerical resolution of discrete integration